Digital holography simulations and experiments to quantify the accuracy of 3D particle location and 2D sizing using a proposed hybrid method

Daniel R. Guildenbecher,[1,*] Jian Gao,[2] Phillip L. Reu,[1] and Jun Chen[2]

[1]Sandia National Laboratories, Albuquerque, New Mexico 87185, USA

[2]School of Mechanical Engineering, Purdue University, West Lafayette, Indiana 47907, USA

*Corresponding author: drguild@sandia.gov

Received 4 February 2013; revised 9 April 2013; accepted 11 April 2013;
posted 11 April 2013 (Doc. ID 184833); published 30 May 2013

The accuracy of digital in-line holography to detect particle position and size within a 3D domain is evaluated with particular focus placed on detection of nonspherical particles. Dimensionless models are proposed for simulation of holograms from single particles, and these models are used to evaluate the uncertainty of existing particle detection methods. From the lessons learned, a new hybrid method is proposed. This method features automatic determination of optimum thresholds, and simulations indicate improved accuracy compared to alternative methods. To validate this, experiments are performed using quasi-stationary, 3D particle fields with imposed translations. For the spherical particles considered in experiments, the proposed hybrid method resolves mean particle concentration and size to within 4% of the actual value, while the standard deviation of particle depth is less than two particle diameters. Initial experimental results for nonspherical particles reveal similar performance.

OCIS codes: (090.1995) Digital holography; (350.4990) Particles.
http://dx.doi.org/10.1364/AO.52.003790

1. Introduction

Holography can be used to record and reconstruct the complex amplitude of a 3D optical field [1–3]. In the recording step, both the amplitude and phase information are encoded in a hologram whose transmission function is proportional to the intensity of the interference pattern between the object wave and the reference wave. In the reconstruction step, the interference of the conjugate reference wave and the hologram yields an image of the object wave. This process is illustrated mathematically by [4]

$$E(x,y;z) = [I_0(x,y)E_r^*(x,y)] \otimes g(x,y,z). \quad (1)$$

Here E is the reconstructed complex amplitude, $I_0(x,y)$ is the recorded intensity of the hologram, E_r^* is the conjugate reference wave, $\otimes$ represents the convolution operation, and $g(x,y,z)$, is the Rayleigh–Sommerfeld diffraction kernel with a unit obliquity factor expressed as

$$g(x,y;z) = e^{jk\sqrt{x^2+y^2+z^2}} \Big/ j\lambda\sqrt{x^2+y^2+z^2}. \quad (2)$$

Here λ is the wavelength, k is the wave number, and z is the propagation distance from the hologram. In digital holography, a CCD is used to record the hologram as a digital grayscale image, and thus the cumbersome wet-chemical preprocessing of the hologram in analog holography is eliminated. In

1559-128X/13/163790-12$15.00/0

digital reconstruction, Eq. (1) is solved numerically in the frequency domain by

$$E(x,y,z) = \Im^{-1}\{\Im\{I_0(x,y)\} \cdot G(f_x,f_y;z)\}, \quad (3)$$

where $\Im$ and $\Im^{-1}$ denote the Fourier transform and inverse Fourier transform, respectively. Typically, these transforms are numerically evaluated with the fast Fourier transform (FFT). f_x and f_y are the transverse spatial frequencies, respectively. Finally, $G(f_x,f_y;z) = \exp\{jkz(1-\lambda^2 f_x^2 - \lambda^2 f_y^2)^{1/2}\}$ and is the analytic solution to the Fourier transform of Eq. (2) [4]. Note in this equation, E_r^* is assumed to be a plane reference wave with unit amplitude.

Because of its simplicity, the in-line configuration has been extensively adopted for many practical applications, particularly in the measurement of particle fields [5–29]. Shown in Fig. 1 is a typical experimental configuration. The performance of this technique relies heavily on the accuracy of the measured depth (i.e., focus plane) of the particles. However, due to the limited aperture and the comparatively large pixel size of current imaging sensors, the depth of focus of digital holographic imaging systems is large [3]. This considerably increases the uncertainties in depth measurement. As an example, for size-limited recording, as defined in [30], the depth of focus can be estimated by

$$\delta \approx d^2/\lambda, \quad (4)$$

where d is the particle diameter. For the experimental conditions considered in this work ($d = 465$ μm, $\lambda = 532$ nm), $\delta \approx 0.4$ m. To be of practical use, methods are needed to determine particle depth with uncertainty significantly less than δ. For this reason, the first goal of the current work is to evaluate the accuracy of particle depth detection techniques and propose new techniques with improved accuracy.

In the literature, methods to determine particle depth are often based on either the intensity [5–9] or the sharpness of edges within the reconstructed images [10–13], and it is assumed that in-focus particles are defined by extremes in intensity or edge sharpness with respect to depth. This work focuses on the evaluation and improvement of these types of methods and draws particular inspiration from the work of Tian *et al.* [6]. Note that many alternative methods have been developed for digital holographic microscopy [14–17] where the nature of light scattering by small particles (on the order of micrometer or less) creates unique challenges. Such methods are not considered in detail here.

In addition, for many practical applications, particles are characterized by nonspherical morphologies. However, most particle detection techniques in the literature have been calibrated for detection of spherical particles, and few have been specifically investigated for detection of nonspherical morphologies [11,18,19]. Therefore, the second goal of this work is to quantify the accuracy of particle detection techniques for application to nonspherical particles. Particular attention is placed on the detection of opaque particles, as such particles can be readily modeled and have many practical applications.

This paper begins with the development of a nondimensional model for the formation and reconstruction of synthetic holograms. Models of spherical and rectangular particles are evaluated and compared to existing particle depth determination methods over a wide range of nondimensional parameters. Based on the lessons learned, a new hybrid particle detection method is presented. Finally, the accuracy of the proposed method is experimentally verified for both spherical and nonspherical particles.

2. Theoretical Analysis

A. Methodology

As discussed in the previous section, a number of methods have been proposed for the estimation of particle position and shape from in-line, digital holograms. Here, the accuracy of a few of these methods is evaluated using simulated holograms of individual spherical and nonspherical, absorbing particles. As is often done in the literature [14,20,21], complexities arising from 3D particle morphologies are ignored, and each particle is modeled as a two-dimensional opaque shape.

A simple method for simulation of digital holograms involves the numerical propagation of the complex amplitude from the plane containing the simulated particle to the recording plane using Eq. (3) [7,10,22]. However, errors in the simulated hologram may be introduced due to discretization, the inherent

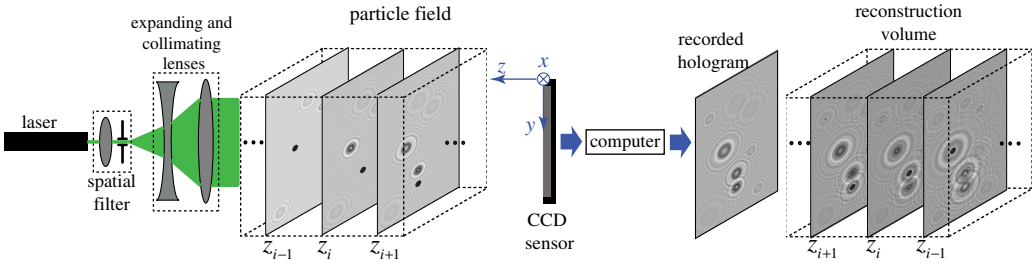

Fig. 1. Schematic of in-line digital holography applied to particle field: (a) recording and (b) reconstruction.

periodicity of the FFT, and signal windowing. In addition to this, Eq. (3) will also later be used for reconstruction of the particle field, and use of the same numerical method for simulation and reconstruction may be problematic. To avoid these issues in this work, simulated holograms are calculated from the analytic solution of the propagation equations. This choice has the additional advantage of yielding a nondimensional model that allows for evaluation of accuracy in terms of nondimensional parameters.

To begin, consider the case of a spherical particle modeled as an opaque disk of radius a_o (in the x–y plane) centered at $(x = 0, y = 0, z = 0)$. It is assumed that the disk is illuminated by a plane reference wave propagating along the z axis with uniform intensity, I_r. An exact analytic solution for the intensity in the recording plane, I_0, at distance z_o based on the solution of Eq. (1) is not available. However, an exact solution to the somewhat simpler Fresnel equation is available and can be written as

$$I_0(\rho; Z_a)/I_r = |1 - j\pi e^{-j\pi\rho^2/Z_a}[L(u,v) - M(u,v)]/Z_a|^2. \tag{5}$$

Here, $I_0(\rho; Z_a)/I_r$ is the nondimensional intensity in the recording plane. $\rho = (x^2 + y^2)^{1/2}/a_o$. $Z_a = \lambda z_o/a_o^2$ and is the inverse of the Fresnel number. $u = 2/Z_a$ and $v = 2\rho/Z_a$. Finally, $L(u,v)$ and $M(u,v)$ are solutions to Lommels' integral of the form $\int_0^1 J_0(v\rho)e^{-ju\rho^2/2}\rho d\rho = [L(u,v) - jM(u,v)]/2$,where J_0 is the zero-order Bessel function of the first kind. The derivation of Eq. (5) is based on the equations presented by Gu and Gan [31,32] and Mielenz [33] for circular apertures combined with Babinet's principle. In the results presented in Section 2B, the numerical method of Mielenz [33] is used to calculate $L(u,v)$ and $M(u,v)$.

Similarly, opaque rectangles of half-width w_o and half-height h_o, located at $(x = 0, y = 0, z = 0)$, are used to model prototypical nonspherical particles. As was the case for the opaque disk, an exact solution to the Fresnel equation can be derived and is given by

$$I_0(X,Y;Z_w,b)/I_r = \left| \begin{array}{l} 1 + \frac{j}{2}\left\{C\left(\sqrt{\frac{2}{Z_w}}(1-X)\right) - C\left(-\sqrt{\frac{2}{Z_w}}(1+X)\right) + j\left[S\left(\sqrt{\frac{2}{Z_w}}(1-X)\right) - S\left(\sqrt{\frac{2}{Z_w}}(1+X)\right)\right]\right\} \\ \times\left\{C\left(b\sqrt{\frac{2}{Z_w}}(1-Y)\right) - C\left(-b\sqrt{\frac{2}{Z_w}}(1+Y)\right) + j\left[S\left(b\sqrt{\frac{2}{Z_w}}(1-Y)\right) - S\left(b\sqrt{\frac{2}{Z_w}}(1+Y)\right)\right]\right\} \end{array} \right|^2. \tag{6}$$

Here, $I_0(X,Y;Z_w b)/I_r$, is the nondimensional intensity in the recording plane. $X = x/w_o$, $Y = y/h_o$, $Z_w = \lambda z_o/w_o^2$, $b = h_o/w_o$ and is the aspect ratio. Finally, $C(\alpha)$ and $S(\alpha)$ are solutions to the integral $\int_0^\alpha e^{j\pi\sigma^2/2}d\sigma = [C(\alpha) + jS(\alpha)]$,and are sometimes referred to as the Fresnel cosine and sine integrals, respectively. The derivation of Eq. (6) is based on the equations presented by Goodman [4] for a square aperture combined with Babinet's principle. In the results presented in Section 2B, the numerical method of D'Errico [34] is used to calculate $C(\alpha)$ and $S(\alpha)$.

Equations (5) and (6) provide an exact, nondimensional expression for the intensity at the recording plane due to an opaque disk and opaque rectangle, respectively. Next, the intensity is assumed to be sampled by a CCD with N pixels in the x-direction and M pixels in the y-direction, where the active area of each pixel is assumed to be of size $\Delta x \times \Delta y$. In a nondimensional form, this pixel size is given by $\Delta x/a_o \times \Delta y/a_o$ or $\Delta x/w_o \times \Delta y/h_o$ when modeling the disk or rectangle, respectively. In the results presented in the Section 2B, a 100% fill factor is assumed such that the active area and physical size of each pixel is the same. Finally, to model the local signal averaging at each pixel, the exact nondimensional intensity is calculated on a grid which is ten times finer than the nondimensional CCD grid, and then averaged onto the CCD grid.

Next, the effects of some important noise sources are added to the modeled signal. First, it is assumed that the CCD converts the analog signal to a digital signal with n bits of accuracy. It is further assumed that the constant reference intensity, I_r, is converted to a digital value given by $\gamma[2^n - 1]$, where γ is the percent of the full-scale output. Therefore, the effects of analog to digital conversion are introduced by scaling the nondimensional intensity by $\gamma[2^n - 1]$ and rounding to the nearest integer value. Second, to model the effects of shot noise, thermally generated noise, readout noise, and other random noise sources, normally distributed random integer values with a mean of zero, and a standard deviation of $\beta[2^n - 1]$ are added to all of the simulated pixel values. Here, β is the standard deviation of the noise as a percent of full-scale output.

In summary, the preceding discussion outlines a nondimensional model for hologram formation and recording when the object is a single opaque disk of radius a_o or a rectangle of half-width w_o and half-height h_o. The relevant nondimensional parameters are (1) $Z_a = \lambda z_o/a_o^2$ or $Z_w = \lambda z_o/w_o^2$ for the disk and rectangle, respectively, which can be considered as a nondimensional recording distance; (2) $b = h_o/w_o$, which defines the aspect ratio of the rectangle; (3) γ, which quantifies the nondimensional reference

intensity; (4) $\Delta x/a_o$ and $\Delta y/a_o$ or $\Delta x/w_o$ and $\Delta y/h_o$, which are the nondimensional pixel sizes; (5) N, which is the number of pixels in the x-direction; (6) M, which is the number of pixels in the y-direction; (7) n, which is the number of bits for analog to digital conversion; (8) β the nondimensional standard distribution of CCD noise.

To apply this model, it is also necessary to nondimensionalize the reconstruction equation. As mentioned in Section 1, the discrete form of the Rayleigh–Sommerfeld equation, Eq. (3), is often used to calculate the reconstructed signal. However, nondimensionalization of Eq. (3) requires the definition of yet another nondimensional parameter. To avoid further increasing the parameter space when performing reconstruction of the simulations in this section, the Fresnel equation is utilized for reconstruction rather than Eq. (3). By applying the same nondimensional parameters as above, the discrete Fresnel equation, in convolution form, can be written as

$$I(X,Y;Z,b)/I_r = |\Im^{-1}\{\Im\{I_0(X,Y;Z,b)/I_r\} \cdot G(f_X,f_Y;Z,b)\}|^2, \quad (7)$$

where $I(X,Y;Z,b)/I_r$ is the intensity in the reconstruction plane, and $G(f_X,f_YZ,b) = \exp\{-j\pi Z[(f_X)^2 + (f_Y/b)^2]\}$. When evaluating Eq. (7) for the disk, $Z = \lambda z/a_o^2$ and $b = 1$ and for the rectangle, $Z = \lambda z/w_o^2$ and $b = h_o/w_o$. Notice that no additional nondimensional parameters are required to evaluate Eq. (7).

Equations (5)–(7) define a model for hologram formation, recording, and reconstruction in terms of nondimensional parameters. These equations are programmed and evaluated with a MATLAB script. In the results presented in Section 2B, six test cases are considered with the relevant parameters defined in Table 1. These parameters are selected to span the range of conditions considered in the experiments and other conditions expected in the intended application. For each test case, 20 different values of Z are simulated, and at each value of Z, 20 separate holograms are calculated to allow for evaluations of the effects of the random noise on reconstruction accuracy. In total, 2400 separate hologram simulations are performed.

Two methods to detect particle shape and position are evaluated: (1) particle detection based on intensity minimization in the depth direction and (2) particle detection based on maximum edge sharpness in the depth direction. For both methods, the intensity is reconstructed at 1000 planes at depths between $0.9Z_o$ and $1.1Z_o$ where Z_o is the actual value of Z_a or Z_w.

The minimum intensity method is based on the assumption that intensity within a reconstructed particle is minimized at the in-focus plane. To implement this method, the minimum intensity value and its corresponding Z location for each pixel are stored to form a minimum intensity map. Particles are detected by applying a threshold to the minimum intensity values, and depth is estimated by the mean Z location of minimum intensity within the detected particles.

In the maximum edge sharpness method, particles are assumed to be in-focus when the sharpness of their edge is maximized. Sharpness is quantified by the Tenengrad operator applied to each pixel in the reconstructed image, where the Tenengrad operator is defined as

$$T(x,y) = [A(x,y) \otimes S_x]^2 + [A(x,y) \otimes S_y]^2. \quad (8)$$

Here $A(x,y)$ is the reconstructed amplitude, defined as the square root of intensity. S_x and S_y are the horizontal and vertical Sobel kernels, respectively [35]. (Note that in a previous publication the Tenengrad operator was applied to the intensity image rather than the amplitude as proposed here [23]; however, through trial-and-error it is found that the amplitude produces a Tenengrad map with higher-signal to noise.) To apply this method, Eq. (8) is solved to find the value of the Tenengrad operator for each pixel at all values of Z. Next, the maximum Tenengrad value and its corresponding Z location are stored to form the maximum Tenengrad map. Finally, a threshold is applied such that any pixel with maximum Tenengrad value greater than the threshold is assumed to form an in-focus edge. The depth of the in-focus edge is taken as the mean Z location of maximum Tenengrad within the detected particles.

B. Results and Discussion

An evaluation of the conditions and methods outlined in the previous subsection results in a significant amount of data. Detailed presentation and discussion of these data, in their entirety, are beyond the scope of this work. Here a few select results are presented to illustrate the important trends.

Figure 2 shows the minimum intensity and maximum Tenengrad maps for the case of the large square at $Z_o = 2.979$. Figures 2(a) and 2(b) show the

Table 1. Nondimensional Conditions Considered in Simulations of Digital Holograms

Description	Z_a or Z_w	b	γ	$\Delta x/a_o$ or $\Delta x/w_o$	$\Delta y/a_o$ or $\Delta y/h_o$	N	M	n	β
Large disk	$0.425 \le Z_a \le 8.512$	N/A	0.5	0.0296	0.0296	1024	1024	14	0.006
Large square	$0.425 \le Z_w \le 8.512$	1	0.5	0.0296	0.0296	1024	1024	14	0.006
Large rectangle	$0.425 \le Z_w \le 8.512$	2	0.5	0.0296	0.0148	1024	1024	14	0.006
Small disk	$10.64 \le Z_a \le 212.8$	N/A	0.5	0.148	0.148	1024	1024	14	0.006
Small square	$10.64 \le Z_w \le 212.8$	1	0.5	0.148	0.148	1024	1024	14	0.006
Small rectangle	$10.64 \le Z_w \le 212.8$	2	0.5	0.148	0.074	1024	1024	14	0.006

value and Z location of minimum intensity, respectively, while Figs. 2(c) and 2(d) show the value and Z location of maximum Tenengrad. To detect objects, these images in Figs. 2(a) and 2(c) are thresholds, resulting in the detected regions shown in Fig. 3. Note that the x and y axis in Fig. 3 have been reduced compared to Fig. 2 to better illustrate the results. Also, in Fig. 3(b) the specified threshold is defined as a percent of the overall maximum Tenengrad value.

To estimate the particle depth, the Z locations of the minimum intensity and maximum Tenengrad for all pixels within the detected regions are averaged together. The errors in the detected depths for all conditions considered for the large square test case are summarized in Fig. 4. In this figure, lines show the mean value of the detected depth for all 20 realizations of random noise considered at each condition, and the error bars represent the standard deviation.

For spherical particles, Tian *et al.* proposed a related minimum intensity method where depth is calculated from the edge pixels of the thresholded minimum intensity map [6]. That method has also been evaluated using the procedures outlined in this section, and it is found to indeed produce superior results when applied to the disk. However, when applied to square and rectangular particles, the depth error is larger than that shown in Fig. 4(a).

From Figs. 3 and 4, it is seen that the accuracy of the detected particle shape and position is a strong function of the selected algorithm and applied threshold. Results for all other conditions outlined in Table 1 show similar trends. In general, the minimum intensity method is superior for detecting a single, connected region from which particle shape and in-plane position can be measured [see Fig. 3(a)]. In contrast, particle outlines detected with the maximum Tenengrad method often contain holes that complicate efforts to extract the particle shape [see Fig. 3(b)]. On the other hand, as seen in Fig. 4, with relatively high thresholds, the maximum Tenengrad method is superior to the minimum intensity method for determination of particle depth.

A few important limitations of these methods should be highlighted: first, the optimum thresholds are a strong function of particle size and shape. For applications where a broad distribution of size and shape is expected, the use of a single threshold to detect all particles is unlikely to result in accurate results. Second, for the case of the symmetric disks, the Tenengrad method fails to accurately detect particle depth. This is attributed to the presence of Poisson's spot, which leads to large spatial gradients (high Tenengrad operator) within the particle interior and consequently the detection of false edges. Third and final, the results tend to be somewhat unstable, such that thresholds that give reasonable results at one value of Z_o may produce large errors at slightly different values of Z_o.

In summary, this section outlines simulation procedures to evaluate the accuracy of particle detection algorithms. Unlike other methods commonly found in the literature, governing equations are fully nondimensional, care has been taken to ensure high accuracy of the simulated holograms, and estimates for uncertainty are included. Results indicate the

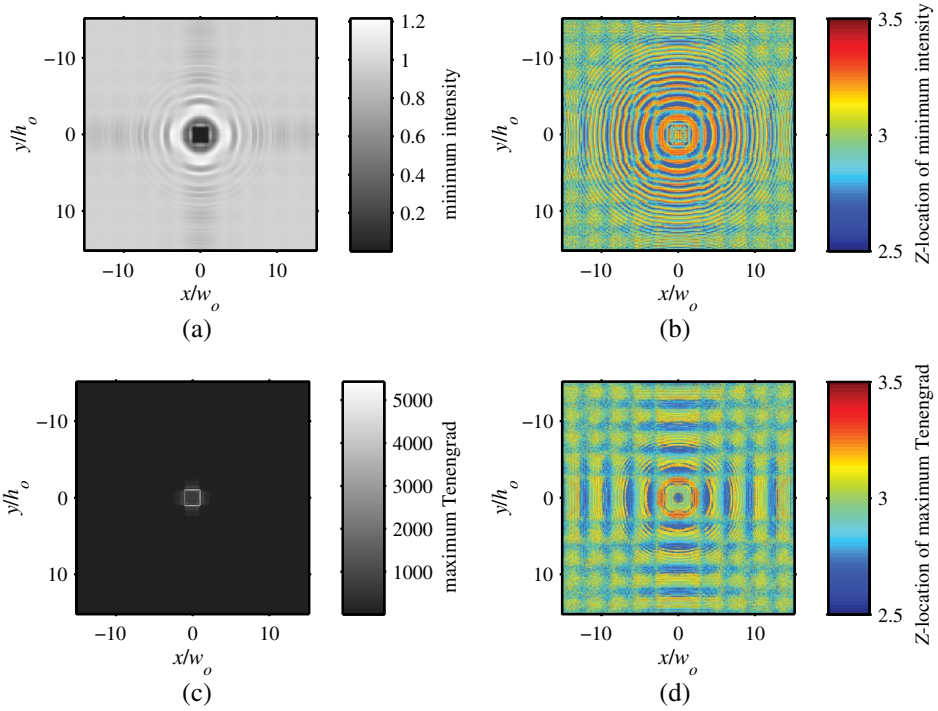

Fig. 2. (a) Minimum intensity in the reconstructed Z direction and (b) the corresponding Z location. (c) Maximum Tenengrad in the Z direction and (d) corresponding Z location for the large square at $Z_o = 2.979$.

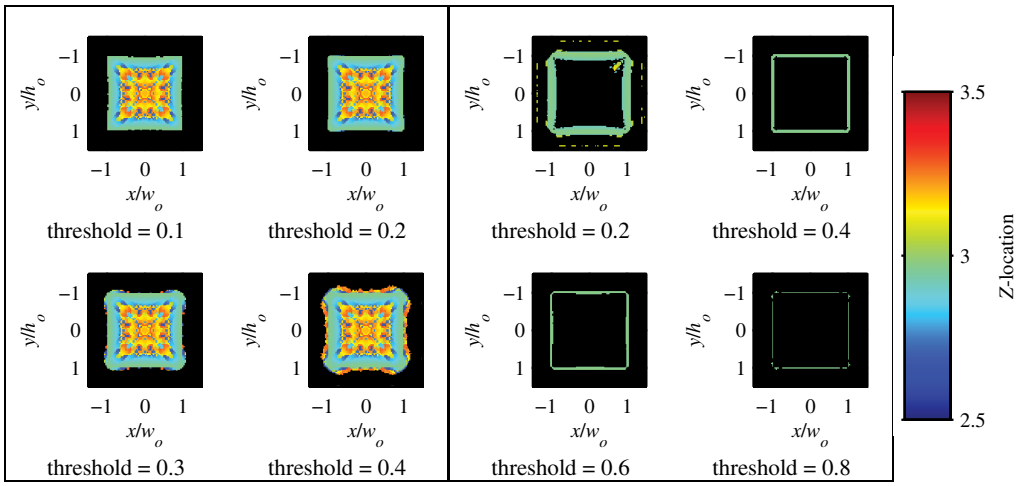

Fig. 3. Detected particle regions from: (a) thresholded minimum intensity and (b) thresholded maximum Tenengrad maps given in Fig. 2. Note, the correct shape is a square of unit extent. Color indicates the detected Z location of each pixel. Artifacts in the upper-left Fig. (b) result from noise added to the simulated hologram.

simulations are useful for exploring a wide range of conditions. In Section 3, these procedures will be further applied for evaluation of the accuracy of a proposed hybrid particle detection method based on a combination of the minimum intensity and maximum Tenengrad methods. This hybrid method is specifically designed to overcome the limitations discussed in the previous paragraph.

3. Proposed Hybrid Particle Detection Method

As discussed in Section 2B, with an optimum threshold, the minimum intensity map tends to produce accurate representations of the particle shape and in-plane position. On the other hand, when particle edges are accurately captured, the thresholded maximum Tenengrad map tends to better capture the particle depth. To combine these two methods, it is proposed to apply various thresholds to the minimum intensity map to find a family of possible particle edges. Then, the values of the Tenengrad map from the pixels on the particle edge are averaged to estimate the edge sharpness of each possible particle edge. Finally, the particle edge with the maximum Tenengrad operator is chosen as the in-focus edge, and its depth is calculated from the average Z location along the selected edge of the Tenengrad depth map.

The Tenengrad operator tends to maximize on a boundary that is slightly outside of the actual particle edge. This is likely related to the ringing effect in coherent imaging in which the image of an opaque disk displays higher spatial gradients just outside its edge (see Fig. 6.20 in [4]). For the conditions considered here, this effect is reasonably accounted for by dilating the thresholded minimum intensity map outward by one pixel before calculating the average Tenengrad operator along the detected edge.

This hybrid method is evaluated for the test cases given in Table 1. For all conditions, the minimum intensity and maximum Tenengrad maps are calculated from the reconstruction of 1000 planes at depths between $0.9Z_o$ and $1.1Z_o$. One hundred different potential particle edges are considered by thresholding the minimum intensity between 0.001 and 0.7.

Figure 5 illustrates the results when applied to the case of the large square at $Z_o = 2.979$. Figure 5(a) shows the average of the Tenengrad map calculated for each threshold. From this it is seen that a threshold of 0.1352 gives the highest mean value of the

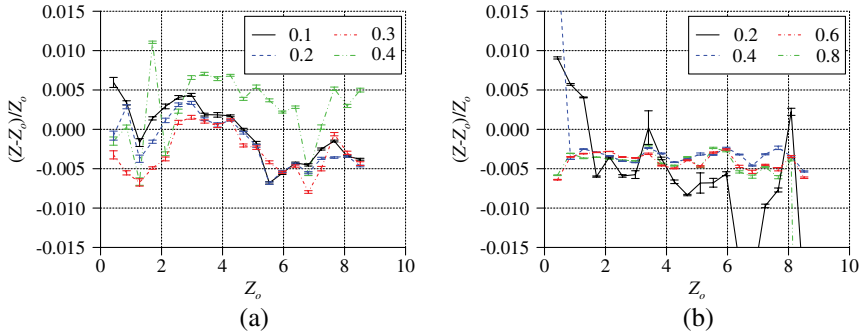

Fig. 4. Error in detected depth from: (a) the thresholded minimum intensity and (b) the thresholded maximum Tenengrad maps given in Fig. 2. Error bars indicate the standard distribution. Legend indicates the value of the applied threshold.

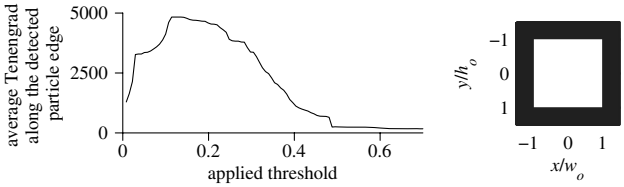

Fig. 5. Illustration of hybrid particle detection method applied to the simulated large square test case at $Z_o = 2.9973$. (a) Average of the Tenengrad map along the detected edges from the thresholded minimum intensity map and (b) image of the in-focus particle at the detected optimum threshold.

Tenengrad operator and is used to find the in-focus particle shape shown in Fig. 5(b). For this case, the detected nondimensional particle Z position is 2.966, an error of −0.42% with respect to the actual value. In addition, the detected particle height and width is 0.977, an error of −2.32% with respect to the actual value.

Figure 6 summarizes the accuracy of the hybrid method for all conditions given in Table 1. Comparison of Fig. 6(a) with Fig. 4 reveals that the accuracy in detected depth is significantly improved compared to the minimum intensity or maximum Tenengrad methods. In addition, the results are relatively stable, in that small changes in particle position do not lead to large changes in accuracy. Finally, it is important to reiterate that the proposed hybrid method does not require *a priori* knowledge of the optimum threshold, a significant improvement over previous methods.

Figures 6(b)–6(d) shows the error in the detected particle diameter, width, and height, respectively, where d_o, w_o, and h_o represent the actual values of diameter, width, and height, respectively. For the large particles, the size error is generally less than about ±5%, which may be acceptable for some applications. However, the size error of smaller particles can exceed ±30%. Similar results have been observed by other authors using alternative algorithms, and when particles are assumed spherical, some authors have chosen to correct experimental results based on trends observed in simulations [24]. No such correction is proposed here, because algorithms are specifically sought that do not require *a priori* knowledge of particle shape.

To improve the detection of small, nonspherical particles, a second depth refinement may be performed, repeating the process as described above with the exception that the intensity reconstructed at the current best estimate of particle location is thresholded to find the family of possible particle edges rather than the minimum intensity. For example, Fig. 7 summarizes the results after applying a second refinement to the small rectangle test case. Significant improvement is achieved in the detected depth and width. Note that further iterations of this process are possible, but simulations indicate little change in results after the second refinement. Also, for the other test cases listed in Table 1, the change in accuracy after applying a second refinement is less. Nevertheless, the results in Fig. 7 indicate that further refinement of particle shapes via the

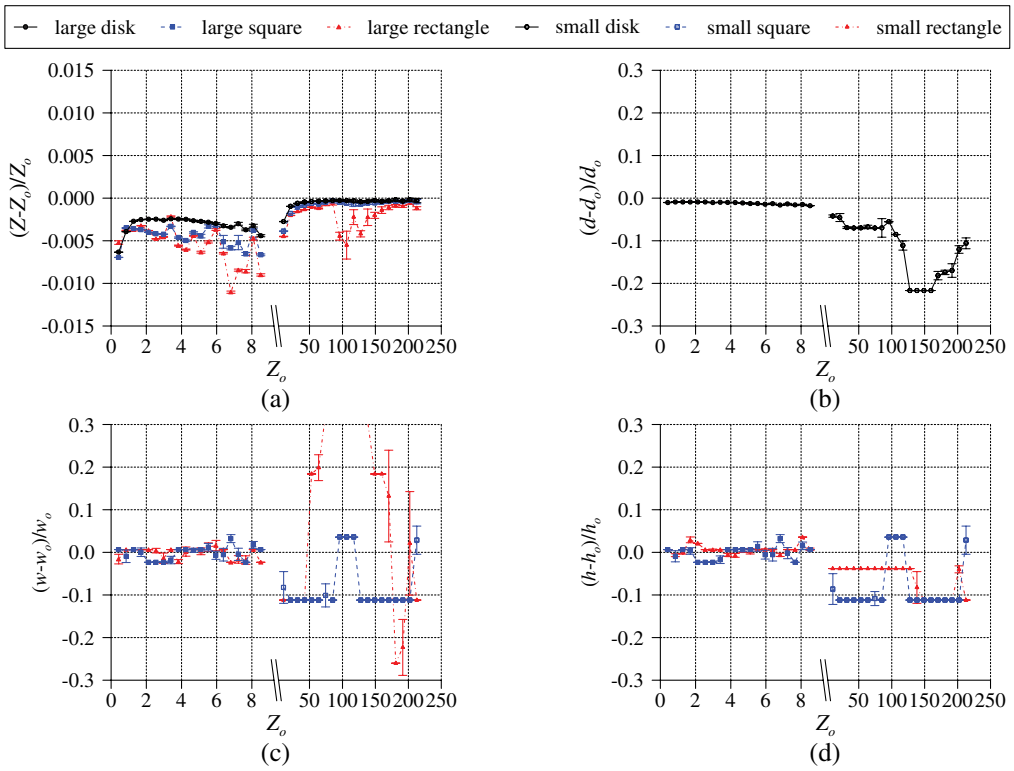

Fig. 6. Error in detected particle: (a) depth, (b) diameter, (c) width, and (d) height for the proposed hybrid method. Error bars indicate the standard distribution.

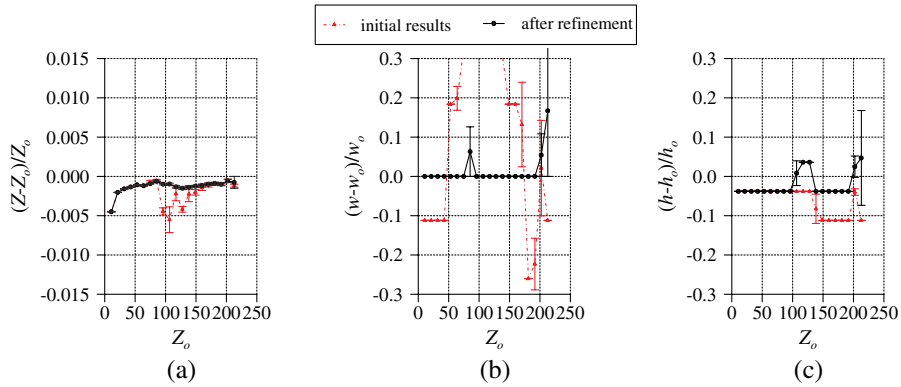

Fig. 7. Error in detected particle: (a) depth, (b) width, and (c) height for the small rectangle test case after a second refinement where the intensity at the Z location from the first iteration is thresholded to find particle images. Error bars indicate the standard distribution.

thresholded local intensity may be advantageous for certain conditions.

Finally, it should be noted that the proposed hybrid method makes no attempt to eliminate the out-of-focus twin-images which add noise around the reconstructed particle images [3]. For applications to dense fields of small particles where $Z \gg 1$, reduction of the twin-image effect may be possible using methods proposed in the literature [36,37]; however, it is left as future work to explore these methods.

4. Experimental Analysis

Experiments are performed to validate the theoretical analysis and quantify any additional sources of experimental uncertainty. This section begins with an overview of the experimental setup followed by discussion of experimental results for spherical particles. Finally, initial results for nonspherical particles are presented.

A. Methodology

The experimental configuration is illustrated in Fig. 8. A frequency doubled, continuous wave, Coherent Verdi V6 Nd:YAG laser is spatially filtered and collimated to form the reference wave for an in-line digital holography configuration. This illuminates an optical glass cuvette with inner dimensions of 50 mm × 50 mm × 50 mm (Hellma Analytics model 704.003-OG) filled with 100 ml of 10,000 cSt Dow Corning silicone oil. Polystyrene beads from Polysciences, Inc. are added to the silicone oil to serve as the objects of interest. The resulting diffraction pattern is recorded by a Redlake EC16000 MegaPlus II monochrome camera placed at approximately $z_{\text{mean}} \approx 195$ mm from the center of the cuvette. The CCD has 4872 pixels in the x direction and 3248 pixels in the y direction. Each pixel is approximately 7.4 μm square. In the reconstructions presented in Section 4B, the pixel fill factor is assumed to be 100%. Finally, the cuvette is placed on a linear traverse stage oriented in the z direction with a specified positing accuracy of ±3 μm.

In an experiment, the linear traverse stage is used to displace the particle-filled cuvette by 2 mm between each hologram recording. As is shown in Section 4B, particle matching between subsequent reconstructions is used to quantify the experimental accuracy of the particle depth determination algorithms. To improve statistical convergence, the experiments are repeated after stirring the cuvette and degassing in a vacuum to remove any bubbles. In total, 14 experimental holograms are recorded.

The size distribution of the polystyrene beads was independently measured with a Malvern Mastersizer 2000, and the mass median diameter of the particles was found to be approximately 465 μm. Assuming Stokes flow and material properties provided by the manufactures, the settling velocity of the particles is estimated to be 0.84 μm/s. The time necessary to acquire two subsequent holograms is less than 60 s, such that the particles are estimated to settle less than 50 μm in the y direction between acquisitions.

Based on the mass median diameter and the estimated mean depth, the relevant nondimensional parameters are $Z_a \approx 1.9$ and $\Delta x/a \approx \Delta y/a \approx 0.03$.

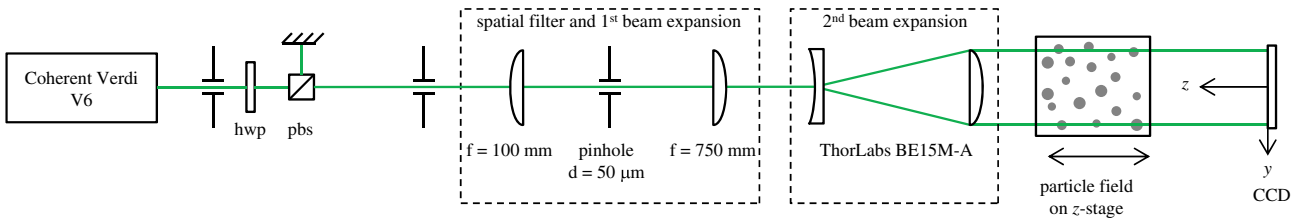

Fig. 8. Experimental configuration for in-line digital holography of a calibration particle field. (hwp, half-wave plate; pbs, polarizing beam splitter).

Holograms are recorded with $n = 14$ bits of accuracy and the reference intensity is adjusted such that the ratio of the recorded reference intensity to the maximum pixel value is approximately $\gamma = 0.5$. Comparison of the aforementioned nondimensional parameters with the conditions defined in Table 1 reveals that the experimental conditions most closely correspond to the large disk simulations. Therefore, the predicted experimental uncertainty is defined by the black lines at $Z_o = 1.9$ in Figs. 6(a) and 6(b).

B. Results and Discussion

Figure 9 illustrates the processing of an experimental hologram using the proposed hybrid method. Figure 9(a) shows an example experimental hologram. Minimum intensity and maximum Tenengrad maps are calculated from reconstruction of 1000 planes at depths between 150 and 250 mm, and the results are shown in Figs. 9(b) and 9(c). Next, the hybrid detection algorithm is applied to find the best estimate of the in-focus particle positions. Here thresholds to the minimum intensity map between 5 and 300 are considered. To account for loss of spatial information and accuracy near the edge of the hologram, no particles are accepted within 200 pixels of the hologram edges. Finally Fig. 9(d) shows the detected shapes of the in-focus particles colored by the detected z position. Despite a large amount of noise in the background of Fig. 9(c), spherical particles are successfully extracted using the hybrid method. Note that although the entire hologram is processed in the described manner, only the center 2056×2056 pixels are shown in Fig. 9 to illustrate features.

On average, 65 particles are detected in each hologram within a volume that is roughly 24 cm^3. This corresponds to a detected particle concentration of 2.7 particles/cm^3. The actual particle concentration is estimated to be 2.8 particles/cm^3 based on the mass of particles added to the silicone oil. The particle size distribution is measured with the Mastersizer, and the material density provided by the manufacturer.

Figure 10 summarizes the particle-size distribution calculated from all particles detected in all holograms. The experimental results are converted to a volume weighted distribution using the detected diameter and assuming spherical particles. Also shown is the particle size distribution measured with the Mastersizer. The mass median diameter measured with holography is 474 μm, a bias of 2.0% with respect to the value measured with the Mastersizer.

To quantify the accuracy of the detected z position, particle matching is performed between successive holograms using a Hungarian routine, which attempts to minimize the sum of the detected displacements [38]. All matching is performed by considering the x, y positions, and to minimize false particle matches, no match is accepted that has a total x, y displacement greater than 100 μm. The results are summarized in Fig. 11. The mean detected displacement is 1.91 mm, while the standard deviation of displacement 0.81 mm. Here, the uncertainty of particle displacements, as quantified by the standard deviation, is 1.74 times

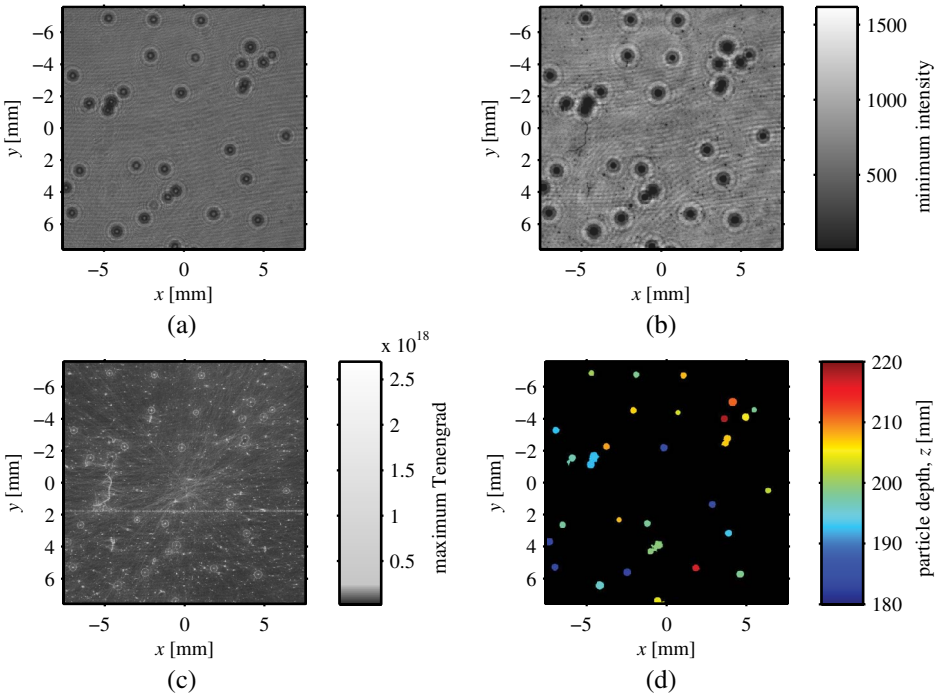

Fig. 9. (a) Experimental hologram of spherical particles, (b) minimum intensity in the reconstructed z direction, (c) maximum Tenengrad in the z direction (scale adjusted to improve visibility of features), and (d) detected in-focus particle shapes colored by detected z location in millimeters.

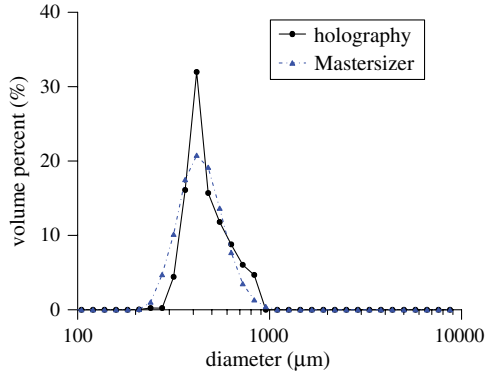

Fig. 10. Comparison of the particle size distribution of the spherical particles measured with holography and the distribution measured with the Malvern Mastersizer 2000.

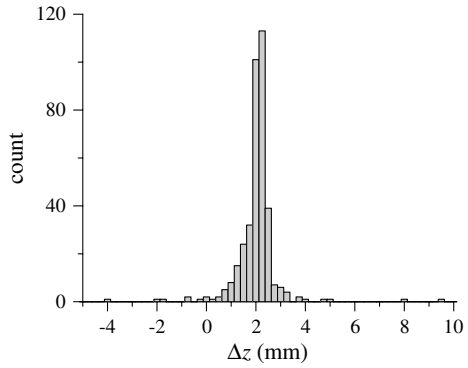

Fig. 11. Histogram of the measured displacements for the spherical particles.

the mean particle diameter. Although few works in the literature have quantified experimental depth uncertainty to the extent reported here, those works that do report distributions of particle positions indicate typical uncertainties on the order of two times the mean particle diameter or greater [25,29].

These results indicate that the hybrid method can successfully extract particle x, y, z position and shape from a 3D particle field. The particle concentration and size distribution closely matches the expected value, while the uncertainty of particle displacements is equal to or better than many results reported in the literature. Furthermore, the hybrid method does not depend on user-defined thresholds and is therefore expected to remain accurate over a broad range of conditions. Nevertheless, some areas for improvement can be noted. For example, the mean diameter is slightly larger than expected. This may be attributed to particles that are closely spaced in the x–y plane and are incorrectly detected as single large particles [see Fig. 9(d)]. Furthermore, the simulations, which consider the effect of camera readout noise on uncertainty, predict a standard deviation of particle z position on the order of 0.001% of z_o, while the experimental value is 0.4% of z_{mean}. Potential sources of experimental uncertainty that are not included in simulations include dust on the beam forming optics, imperfections in the planar wavefront, false detection of closely spaced particles, etc. It seems likely that these experimental noise sources are significantly greater than camera induced noise, and further efforts are need to quantify, model, and reduce their effects. For example, when particle matching is performed on only those particles with detected diameter less than 400 μm, which tends to eliminate large overlapping particles, the mean and standard deviation of displacement improves to 1.95 and 0.42 mm, respectively. This indicates that new algorithms to separate overlapping particles would significantly improve experimental uncertainty. One example is the method using Gaussian mixture models presented by Tian *et al.* [6].

C. Initial Experimental Results for Nonspherical Particles

Finally, the proposed method is tested on a particle field containing nonspherical particles. To do so, the cuvette is placed at approximately $z_{\text{mean}} \approx 300$ mm and is filled with 60,000 cSt silicone oil containing a few metal shavings. Seven holograms are obtained while displacing the cuvette 2 mm in the z direction between recordings. Figure 12(a) shows an example hologram, and Fig. 12(b) shows the particles detected using the hybrid method. Nonspherical shapes are clearly visible, while some spherical particles are also observed and can be attributed to gas bubbles in the highly viscous liquid.

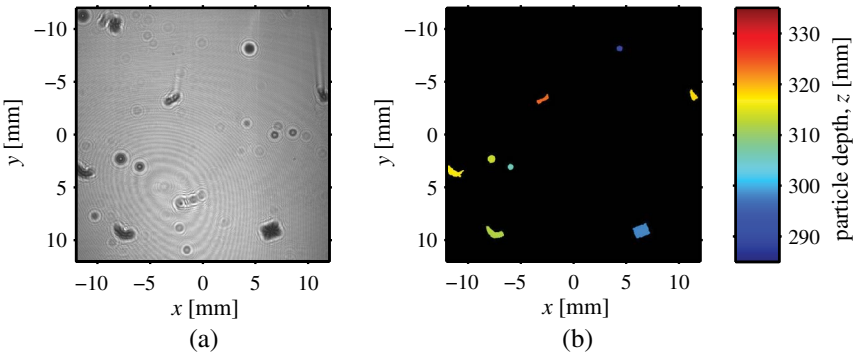

Fig. 12. Example nonspherical particle results showing: (a) the hologram and (b) the detected in-focus particle shapes colored by detected z location in millimeters.

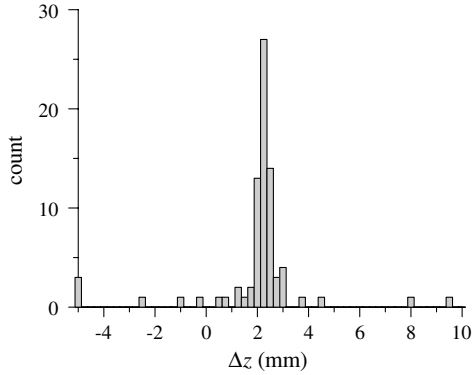

Fig. 13. Histogram of the measured displacements for the nonspherical particles.

Once again, particle matching is performed between subsequent recordings and the results are summarized in Fig. 13. The mean detected displacement is 2.0 mm, while the standard deviation of displacement 3.0 mm. For these particles, the detected area equivalent mean diameter is approximately 860 μm; therefore, the uncertainty of particle displacement is roughly 3.5 times the mean particle diameter. Further experimental data is needed to better resolve the statistics; nevertheless, these initial results indicate that the hybrid method can be successfully applied to nonspherical particles yielding uncertainty similar to that of spherical particles.

5. Conclusions

Among available particle diagnostic techniques, inline digital holography is uniquely suited to capture the 3D spatial distribution of particle position and shape. However, accurate detection of particles is complicated by the large depth of focus.

This work presents a theoretical and experimental evaluation of particle detection methods with particular focus on detection of nonspherical particles. New simulation techniques are developed to accurately model hologram formation and reconstruction of single opaque spherical and rectangular particles. This model is used to evaluate particle detection algorithms based on intensity minimization and edge sharpness maximization. Lessons learned from these evaluations leads to the proposal of a new hybrid method with a number of advantages. Finally, experimental results of spherical and nonspherical particles suspended in a viscous liquid are used to verify the accuracy of the proposed hybrid detection method.

This work has resulted in a number of important findings, including:

- New methods proposed for the simulation of digital holography are fully nondimensional. As shown here, the use of the nondimensional methods allows for reduction of the number of simulations necessary to characterize the accuracy of particle detection algorithms.
- A new particle detection algorithm based on the combination of minimum intensity and edge sharpness is shown to capture particle depth and shape with improved accuracy compared to other methods evaluated in this work. In addition, this method requires no *a priori* knowledge of particle shape or optimum threshold. As a consequence, this method appears well suited to the detection of nonspherical particles with a broad size distribution.
- Experiments that involve imposed translations to quasi-stationary particle fields are shown to be well suited for evaluation of the uncertainty of particle detection algorithms.
- The experimental results indicate additional uncertainties not captured by the single particle simulations. In particular, particles that overlap in the x–y plane increase depth-of-focus and particle size uncertainty. Additional work is needed to develop methods that detect and minimize these effects.

The authors would like to thank Daniel J. Scoglietti and Thomas Grasser for help with the optical setup, Lindsay Gloe Hughes for the particle size measurements using the Malvern Mastersizer, and Luke H. Engvall for implementation of the particle matching routines, all are from Sandia National Laboratories. Sandia National Laboratories is a multiprogram laboratory operated by Sandia Corporation, a Lockheed Martin Company, for the United States Department of Energy's National Nuclear Security Administration under contract no. DE-AC04-94AL85000.

References

1. D. Gabor, "A new microscopic principle," Nature **161**, 777–778 (1948).
2. U. Schnars and W. Jueptner, *Digital Holography: Digital Hologram Recording, Numerical Reconstruction, and Related Techniques* (Springer, 2005).
3. J. Katz and J. Sheng, "Applications of holography in fluid mechanics and particle dynamics," Annu. Rev. Fluid Mech. **42**, 531–555 (2010).
4. J. W. Goodman, *Introduction to Fourier Optics*, 2nd ed. (McGraw Hill, 1996).
5. T. Khanam, M. Nurur Rahman, A. Rajendran, V. Kariwala, and A. K. Asundi, "Accurate size measurement of needle-shaped particles using digital holography," Chem. Eng. Sci. **66**, 2699–2706 (2011).
6. L. Tian, N. Loomis, J. A. Domínguez-Caballero, and G. Barbastathis, "Quantitative measurement of size and three-dimensional position of fast-moving bubbles in air-water mixture flows using digital holography," Appl. Opt. **49**, 1549–1554 (2010).
7. D. K. Singh and P. K. Panigrahi, "Improved digital holographic reconstruction algorithm for depth error reduction and elimination of out-of-focus particles," Opt. Express **18**, 2426–2448 (2010).
8. J. Sheng, E. Malkiel, and J. Katz, "Digital holographic microscope for measuring three-dimensional particle distributions and motions," Appl. Opt. **45**, 3893–3901 (2006).
9. M. Malek, D. Allano, S. Coëtmellec, and D. Lebrun, "Digital in-line holography: influence of the shadow density on particle field extraction," Opt. Express **12**, 2270–2279 (2004).
10. Y. Yang, G. Li, L. Tang, and L. Huang, "Integrated gray-level gradient method applied for the extraction of three-dimensional velocity fields of sprays in in-line digital holography," Appl. Opt. **51**, 255–267 (2012).
11. P. F. Jacob, J. S. Timothy, and A. S. Raymond, "Practical methods for automated reconstruction and characterization of

particles in digital in-line holograms," Meas. Sci. Technol. **20**, 075501 (2009).
12. Y.-S. Choi and S.-J. Lee, "Three-dimensional volumetric measurement of red blood cell motion using digital holographic microscopy," Appl. Opt. **48**, 2983–2990 (2009).
13. V. Ilchenko, T. Lex, and T. Sattelmayer, "Depth position detection of the particles in digital holographic particle image velocimetry," in *Fundamental Problems of Optoelectronics and Microelectronics II* (SPIE, 2005).
14. Y. Park, G. Popescu, K. Badizadegan, R. R. Dasari, and M. S. Feld, "Fresnel particle tracing in three dimensions using diffraction phase microscopy," Opt. Lett. **32**, 811–813 (2007).
15. F. C. Cheong, B. J. Krishnatreya, and D. G. Grier, "Strategies for three-dimensional particle tracking with holographic video microscopy," Opt. Express **18**, 13563–13573 (2010).
16. L. Dixon, F. C. Cheong, and D. G. Grier, "Holographic deconvolution microscopy for high-resolution particle tracking," Opt. Express **19**, 16410–16417 (2011).
17. L. Wilson and R. Zhang, "3D localization of weak scatterers in digital holographic microscopy using Rayleigh–Sommerfeld back-propagation," Opt. Express **20**, 16735–16744 (2012).
18. B. Gopalan and J. Katz, "Turbulent shearing of crude oil mixed with dispersants generates long microthreads and microdroplets," Phys. Rev. Lett. **104**, 054501 (2010).
19. J. P. Fugal, R. A. Shaw, E. W. Saw, and A. V. Sergeyev, "Airborne digital holographic system for cloud particle measurements," Appl. Opt. **43**, 5987–5995 (2004).
20. F. Soulez, L. Denis, C. Fournier, É. Thiébaut, and C. Goepfert, "Inverse-problem approach for particle digital holography: accurate location based on local optimization," J. Opt. Soc. Am. A **24**, 1164–1171 (2007).
21. M. Adams, T. Kreis, and W. Jueptner, "Particle analysis with digital holography," Proc. SPIE **4101**, 314–320 (2000).
22. Y. Yang, B.-s. Kang, and Y.-j. Choo, "Application of the correlation coefficient method for determination of the focal plane to digital particle holography," Appl. Opt. **47**, 817–824 (2008).
23. D. R. Guildenbecher, J. Gao, P. L. Reu, and J. Chen, "Digital holography reconstruction algorithms to estimate the morphology and depth of nonspherical, absorbing particles," in *SPIE Optical Engineering + Applications* (SPIE, 2012).
24. S. L. Pu, D. Allano, B. Patte-Rouland, M. Malek, D. Lebrun, and K. F. Cen, "Particle field characterization by digital in-line holography: 3D location and sizing," Exp. Fluids **39**, 1–9 (2005).
25. Y. Wu, X. Wu, Z. Wang, L. Chen, and K. Cen, "Coal powder measurement by digital holography with expanded measurement area," Appl. Opt. **50**, H22–H29 (2011).
26. Y. Yang and B.-s. Kang, "Measurements of the characteristics of spray droplets using in-line digital particle holography," J. Mech. Sci. Tech. **23**, 1670–1679 (2009).
27. Y. Yang and B.-s. Kang, "Experimental validation for the determination of particle positions by the correlation coefficient method in digital particle holography," Appl. Opt. **47**, 5953–5960 (2008).
28. Y. Yang and B.-s. Kang, "Digital particle holographic system for measurements of spray field characteristics," Opt. Laser. Eng. **49**, 1254–1263 (2011).
29. G. Pan and H. Meng, "Digital holography of particle fields: reconstruction by use of complex amplitude," Appl. Opt. **42**, 827–833 (2003).
30. H. Meng, G. Pan, Y. Pu, and S. H. Woodward, "Holographic particle image velocimetry: from film to digital recording," Meas. Sci. Technol. **15**, 673–685 (2004).
31. M. Gu and X. S. Gan, "Fresnel diffraction by circular and serrated apertures illuminated with an ultrashort pulsed-laser beam," J. Opt. Soc. Am. A **13**, 771–778 (1996).
32. M. Gu and X. S. Gan, "Effect of an ultrashort pulse on Fresnel diffraction by a circular opaque disk," Opt. Commun. **125**, 1–4 (1996).
33. K. D. Mielenz, "Algorithms for Fresnel diffraction at rectangular and circular apertures," J. Res. Natl. Bur. Stand. **103**, 497–509 (1998).
34. J. D'Errico, "FresnelS and FresnelC" (May 3, 2012), retrieved April 16 2012, http://www.mathworks.com/matlabcentral/fileexchange/28765-fresnels-and-fresnelc.
35. J. M. Tenenbaum, *Accommodation in Computer Vision* (Stanford University, 1970).
36. G. Koren, F. Polack, and D. Joyeux, "Iterative algorithms for twin-image elimination in in-line holography using finite-support constraints," J. Opt. Soc. Am. A **10**, 423–433 (1993).
37. O. Mudanyali, D. Tseng, C. Oh, S. O. Isikman, I. Sencan, W. Bishara, C. Oztoprak, S. Seo, B. Khademhosseini, and A. Ozcan, "Compact, light-weight, and cost-effective microscope based on lensless incoherent holography for telemedicine applications," Lab Chip **10**, 1417–1428 (2010).
38. J.-Y. Tinevez, "Simple tracker" (August 20, 2012), retrieved December 1 2012, http://www.mathworks.com/matlabcentral/fileexchange/34040-simple-tracker.